Impact of Facility Electrical Boundary Conditions on the Performance of an Electron Cyclotron Resonance Magnetic Nozzle Thruster

IEPC-2022-510

Presented at the 37th International Electric Propulsion Conference
Massachusetts Institute of Technology, Cambridge, MA, USA
June 19-23, 2022

Salvatore S. Baldinucci[1], Sophia Bergmann[2], Jack A. Hondagneu[3], Benjamin Wachs[4] , and Benjamin A. Jorns[5]
University of Michigan, Ann Arbor, Michigan, 48109

The effect of a simulated downstream biased chamber wall on the operation and performance of a 30-watt electron cyclotron resonance thruster is studied. A movable and suspended 1m $\times$ 1m steel foil panel is used to simulate different electrical downstream boundary conditions. Thrust was found to increase 10% as the unbiased panel is removed from downstream of the thruster for 1 sccm flow rate. Biasing the downstream panel relative to the chamber walls showed negligible performance changes despite measurements of significantly changing current collection in the panel from the downstream plasma. Also, thruster body potential increases substantially as the panel is biased to electron collecting. These results seem to indicate that the demagnetized plasma adjusts itself as to accommodate downstream boundary condition bias. A current model is presented to explain this phenomenon and model observed trends in current through the panel and thruster body voltage as a function of panel bias.

I. Nomenclature

m_i	=	ion mass
m_e	=	electron mass
q_e	=	electron charge
I	=	current
ϕ	=	plasma potential
V	=	panel potential
T_e	=	electron temperature
P_{abs}	=	power absorbed by thruster
$\dot{m}$	=	mass flow rate
η	=	thrust efficiency
F_T	=	thrust

II. Introduction

Magnetic nozzles are an attractive option for low power (< 50 W) propulsion applications. These devices operate on the principle of converting random electron thermal energy of a plasma into directed kinetic energy of the ions. The

[1]PhD PreCandidate, Applied Physics, salbal@umich.edu
[2]MSE Student, Department of Aerospace Engineering, boldlygo@umich.edu
[3]MSE Student, Department of Aerospace Engineering, jackhond@umich.edu
[4]PhD Candidate, Department of Aerospace Engineering, bwachs@umich.edu
[5]Associate Professor, Department of Aerospace Engineering, bjorns@umich.edu

generation of this thermal energy is typically achieved by an externally applied radiofrequency field. Once the propellant is heated, a magnetic nozzle then converts electron thermal energy into directed kinetic energy by an ambipolar diffusion process in which ions follow the electrons as they gyrate around expanding magnetic field lines, drifting away from the ionization source and toward a weaker field downstream. Eventually, the plasma must detach from these field lines in order to generate thrust [1, 2].

Magnetic nozzles have several potential advantages for in-space propulsion. For example, they do not require plasma-wetted electrodes, which in principle can lead to extended lifetime of the thruster. They similarly can employ non-traditional reactive propellants such as metal, water, or carbon dioxide, which are attractive storable propellants for small satellite applications [3, 4]. Magnetic nozzles only require a single power supply, which reduces complexity and footprint. Low power nozzles also in principle have lower efficiency loss due to wall diffusion compared to conventional Hall Effect thrusters (HET) and Gridded ion thrusters (GIT) at small scale. This stems from a strong longitudinal magnetic field that reduces the volume to area ratio losses. For these reasons, there has been particular emphasis on creating a more efficient, high specific impulse, low power magnetic nozzle thruster.

The performance of magnetic nozzle thrusters is directly tied to the ability to efficiently heat the electrons. While there are many schemes such as helicon and inductively coupled plasma sources [5–7] to generate and heat a plasma, Electron Cyclotron Resonance (ECR) is particularly attractive for low power propulsion. This heating scheme uses ECR with a microwave power antenna to ionize and heat propellant. Heating is achieved when the frequency of the electromagnetic wave matches the electron cyclotron frequency. It has been shown that ECR can for some plasmas produce extremely high electron temperatures, exceeding 100 eV [8–10]. This type of energization is critical for high-specific impulse magnetic nozzles.

In light of the advantages of ECR as a heating scheme, these thrusters have been investigated for several decades [11]. However, limitations of the power and efficiency of microwave supplies largely curtailed the development of this concept [12]. Recent advancements in the miniaturization of microwave sources have allowed ECR thruster development to resume in the electric propulsion community [2]. Most notably, measurements of thrust from ECR magnetic nozzle thrusters at Office National d'Etudes et de Recherches Aérospatiales (ONERA), have shown thrust efficiencies in excess of 16% and specific impulses of over 1000s in the 20W-40W power range [13].

While efforts continue to improve ECR magnetic nozzle technology for small satellite applications, in parallel, there have been a number of studies that have highlighted the challenges of testing these systems in ground based facilities. For example, it has been shown that the background pressure in the test facility can have a major impact on thruster performance. Vialis demonstrated in 2018 that performance increased as background pressure decreased [14]. This was a particularly notable result as more conventional types of electric propulsion like Hall thrusters exhibit an opposite trend with pressure. In an effort to explain this result, Wachs and Jorns in 2018 performed a detailed study of the impact of background pressure on the magnetic nozzle [15]. They proposed that the pressure-related effects may stem from increased inelastic collisions in the plume and developed a model for this effect.

With this facility effect in mind, in an effort to better improve test environment, researchers at ONERA performed duplicate testing in a larger and small vacuum facilities [13]. Intriguingly, while they found that background pressure was a dominant driver for performance, they also noted that when they artificially raised the pressure in the larger facility to match the smaller facility, they found the performance in the larger facility exceeded the small facility results by about 30%. This raises the possibility that in addition to pressure, electrical boundary conditions may also be a factor influencing thruster performance. This ultimately may be an intuitive finding since it has been suggested [16–18] that the non-local nature of the electron dynamics of these systems may mean the downstream boundary conditions may have an outsized role on the energy balance in the nozzle.

With that said, while it was apparent from these previous studies that the electrical boundary conditions may impact performance, this effect has yet to be systematically investigated. Given the potential of this technology and the importance of finding high fidelity test environments, the need is apparent for a parametric study into the role of electrical boundary conditions on thruster operation.

To this end, this paper is organized in the following way. Sec. 2, we describe the approach we took to simulate and control the downstream electrical boundary conditions. Sec. 3, we discuss the setup of experimental hardware. Sec. 4, we outline the diagnostic tools we used to measure various aspects of the thruster and its dynamics as well as the test environment. Sec. 5, we present the results from our parametric study. Sec. 6, we discuss the implications of the electrical study, we present a current model in an attempt to describe the results, and we consider the role of facility pressure on performance in the context of these results. Sec. 7, we conclude with a summary of the results, its implications, and suggestions for further investigation.

III. Approach to controlling electrical boundary condition

We describe in this section our experimental approach to controlling the downstream electrical boundary condition for an ECR thruster. The geometry of the setup is shown notionally in Fig. 5. In this case, we suspend a 1m by 1m sheet of steel foil in front of the thruster with motion control in the radial and axial directions relative to the thruster. This sheet is used to simulate the metallic chamber wall in front of thrusters such as ours when tested in vacuum chambers. With the ability to move the sheet while in vacuum, we fired the thruster at multiple operating conditions while the sheet was located in various positions relative to the thruster. These sheet locations include 0.7m downstream from thruster exit face, 1.7m downstream, and finally we swung the sheet to the side as to minimize its influence on thruster operation. This is shown schematically in Fig. 1. This enables partial simulation and rapid experimentation of multiple test chamber sizes. As we parametrically vary the thruster operating condition and beam dump location, we can measure key elements of thruster operation including thrust, background pressure, and body potential.

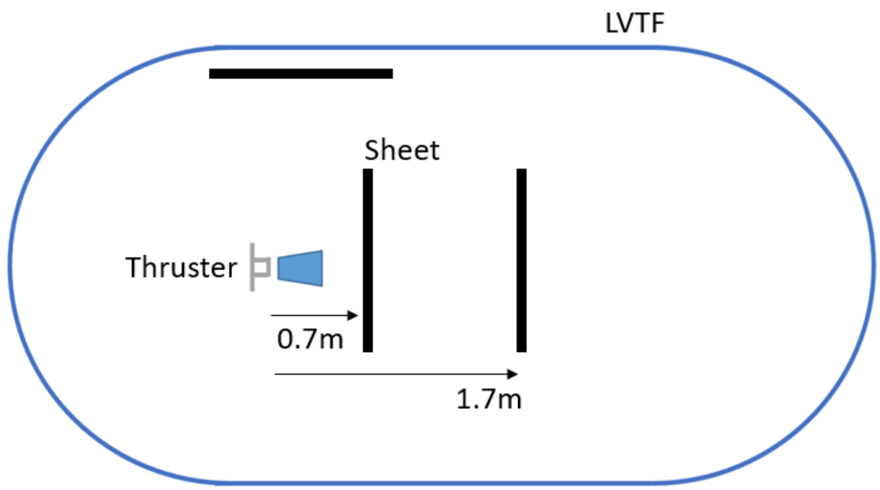

Fig. 1 Sheet locations for different operating points within Large vacuum test facility (LVTF).

We initially grounded the sheet to the chamber wall through an ammeter. This was done in order to simulate the same electrical conditions of the vacuum chamber walls while simultaneously measuring the current through the sheet from the downstream plasma. This allows for determination of thruster operation as a function of downstream chamber wall location. We then electrically isolate the sheet from the chamber walls and attached an external DC power supply in series with the ammeter to the sheet. The electrical diagram for biasing the simulated chamber wall is shown in Fig. 2.

This allowed us to bias the sheet to test how different electrical boundary conditions of a simulated chamber wall affected thruster performance metrics, as well as discern properties such as relative contributions of ion and electron current to thrust. We biased the beam dump while the sheet was located 0.7m downstream of the thruster. This sheet location was chosen as it resembles the proximity to chamber walls in smaller vacuum chambers that these thrusters are often tested within. While sweeping across these voltages we took current measurements revealing an IV curve for the plume. This can be taken and analyzed as a double Langmuir probe relative to the chamber wall in order to obtain plasma properties of the plume. We note that while this steel sheet is useful for simulating boundary conditions of vacuum chambers directly in front of the thruster, it does not encompass all the characteristics such as the curvature and radial boundaries of a real chamber.

IV. Experimental Setup

In this section we describe the prominent experimental equipment used in our parametric investigation. This includes the design architecture of our ECR magnetic nozzle thruster, power and flow systems used to input microwave power to the thruster and provide propellant to the discharge chamber, and the test facility in which we performed the experiments.

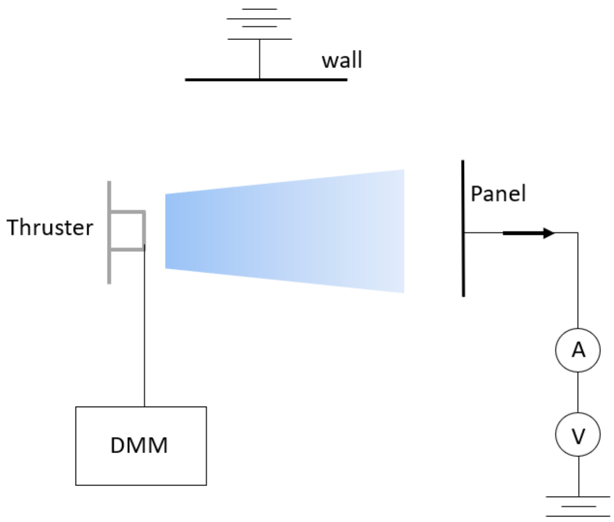

Fig. 2 Electrical schematic for the thruster, chamber wall, and suspended panel.

A. ECR Thruster

The ECR thruster (Fig. 3) we used throughout this test campaign follows the design architecture of the ECR thruster built by ONERA [19], with modifications from Wachs [20]. A coaxial design is implemented in which microwave power is fed by a coaxial line and emitted between a graphite inner antenna and aluminum outer conductor. The outer conductor functions as both a physical boundary of the plasma source region and as a waveguide. Xenon gas is injected radially through twelve injector holes located near the ceramic back plate. NdFeB permanent magnets are used to generate a magnetic field with a peak strength of 1100 Gauss. A global optimization algorithm was performed by Wachs which determined the optimal frequency for this ECR thruster to be 2450 MHz [21]. This frequency corresponds to a resonance zone between the back plane and gas injectors. The resonance zone is the thin region inside the discharge chamber in which the electron cyclotron frequency matches that of the microwave frequency within a specific magnetic field strength. This leads to electron heating and ionization of the neutral gas. It was observed that thruster performance improved with the addition of a layer of boron nitride to the inner region of the outer conductor. Thus, a boron nitride layer is used throughout this campaign. This improvement may suggest the dielectric layer reduces the ion diffusion by blocking current flow through the radial walls [14].

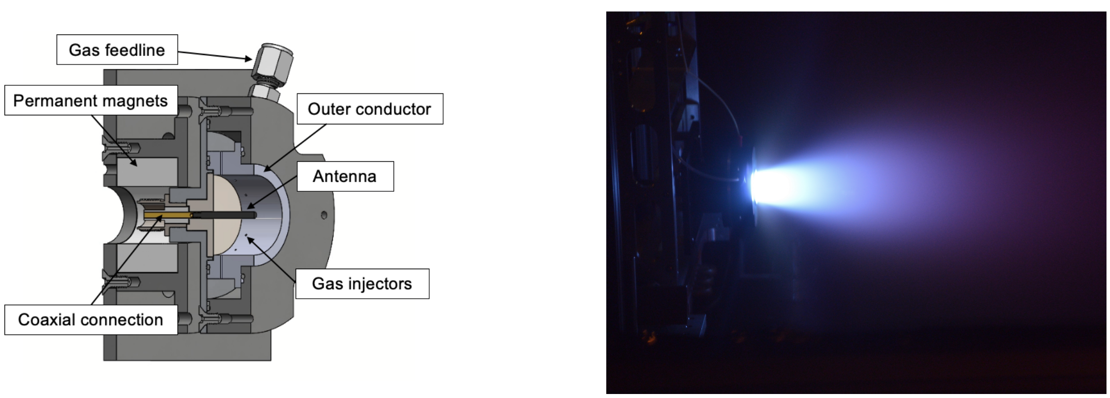

(a) (b)

Fig. 3 (a) ECR thruster cutaway and (b) ECR thruster firing on 1.0 SCCM xenon at 25 W input power at the University of Michigan's test facility.

B. Power and flow

Power input and flow rate are two of the most important aspects to the operation of an ECR magnetic nozzle thruster. It has been shown that variability in these could drastically affect performance metrics and operation of the thruster. To obtain an all encompassing sense of thruster performance in this parametric study we varied flow rate and power input to our thruster. We utilized a flow rate and power test matrix for each panel location inside the test facility. This consisted of flow rates between 0.6-1.5 sccm and power between 20-26 Watts delivered to the thruster. Power limitations of our amplifier as well as cable losses prevented testing at higher powers. Xenon propellant was used for all the experiments in our study. The flow control set up employed an Alicat MCV-10SCCM-D/5M mass flow controller to both set and monitor propellant flow rate. A low-power signal fed into a solid-state power amplifier (Comtech PST ARD88258-50). This amplifier provides the high power microwaves used to power the thruster. This high power signal is then fed through a coaxial cable, connected to a thermocouple-based power sensor (Keysight N8482H) used to measure forward and reverse power to the thruster, then through a vacuum feed through, and finally a wireless coupler which then connects to the thruster. A schematic of the power and propellant delivery systems are shown in Fig. 4.

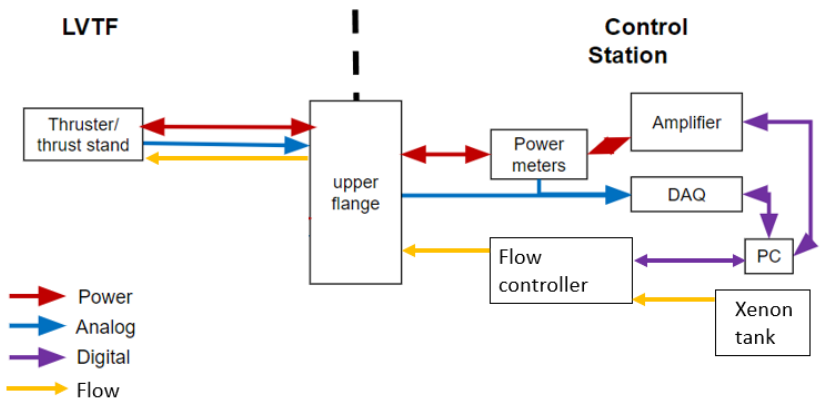

Fig. 4 Power, data, and propellant delivery systems.

The flow controller was calibrated using MesaLabs Definer 220 DryCal system. Our calibrations yielded a mass flow uncertainty of ± 5%. Power uncertainties in our thruster primarily emanate from our directivity errors in the delivered and reflected power. We discuss this more in the appendix.

C. Test facility

We conducted our experiments in the Large Vacuum Test Facility (LVTF) at the University of Michigan's Plasmadynamics and Electric Propulsion Laboratory (PEPL). The setup inside LVTF is shown in Figure 5. The dimensions of the chamber are 9 meters long and 6 meters in diameter. The LVTF pumping system consists of thirteen PHPK-TM1200i re-entrant cryogenic vacuum pumps and six PEPL-developed cryopumps that utilize the Cryomech AL600 Gifford-McMahon. The effecting pumping speed is 500,000 l/s on xenon [22]. The base pressure during experiments varied between 2×10^{-7} Torr-xenon and 3×10^{-7} Torr-xenon. The operating pressure, i.e. when the thruster was firing— varied between 2.5×10^{-7} Torr-xenon and 3×10^{-7} Torr-xenon.

We used Stabil Series 370 Ion Gauges (calibrated for nitrogen) to measure pressure at the chamber wall in LVTF as shown in Fig. 5. Corrections are done in order to convert this to xenon pressure. Its location on the chamber wall will be a accurate measure of pressure within the chamber near the wall. However this does not account for pressure gradients within the chamber nor measure the near plume pressure from the thruster discharge. We return to this point in the discussion.

V. Diagnostics

We provide an overview of the diagnostics used to measure thrust, thruster body potential, and plasma properties. Each of these measurements gives us physical intuition in to how our thruster is operating. This will lead to a more informed discussion of the results.

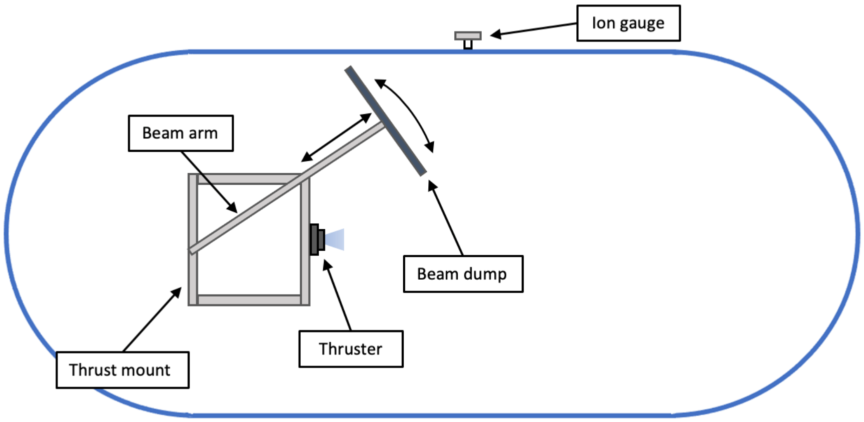

Fig. 5 LVTF experimental setup.

A. Thrust stand

We obtained measurements of thrust and efficiency in this test campaign using the counter weighted hanging pendulum thrust stand described in [21] and [20] and shown in Figure 6. The driver software for this apparatus takes inputs from a fiber-optic displacement sensor mounted on the end of the pendulum arm (Philtec D63), bidirectional thermocouple-based power sensors (Keysight N8482H), and a mass flow controller (Alicat MCV-10SCCM-DISM) averaged over 5 seconds at a rate of 200 Hz to calculate mean values of thrust and efficiency for a single operating point.

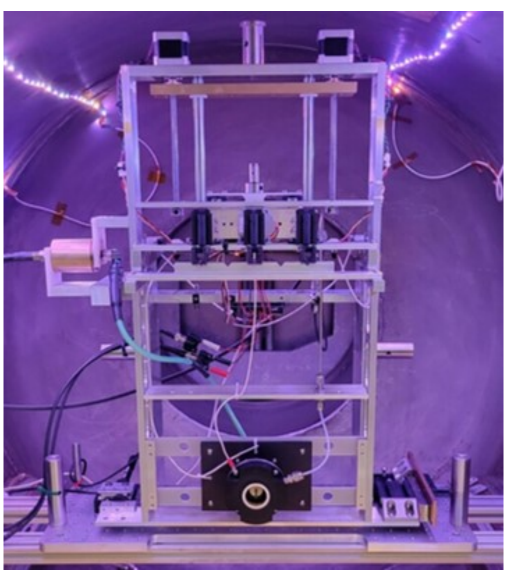

(a)

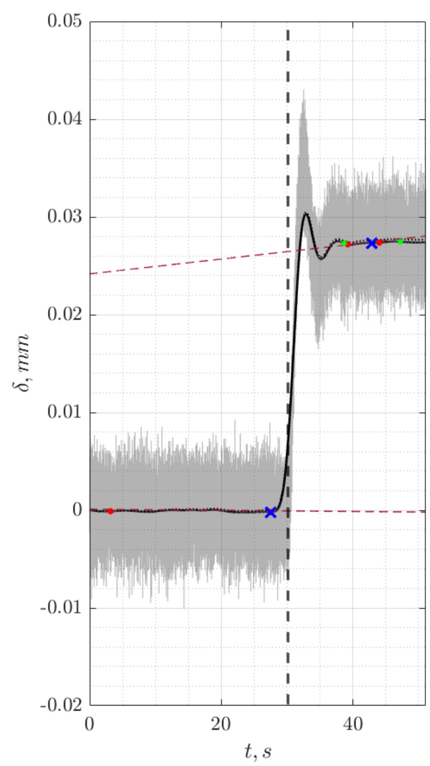

(b)

Fig. 6 (a) ECR thruster mounted on thrust stand and (b) an example of displacement as a function of time during a thrust point measurement. Displacement is correlated with thrust for this system.

This thrust stand employs a known mass calibration system to translate the displacement sensor voltage output to thrust force. We assess the uncertainty in thrust measurements by considering error introduced by the thrust stand elements as well as noise from the surrounding environment. The details of this are included in the Appendix.

B. Body potential

In order to get a sense of plasma potential upstream near the thruster body we attached an electrode to the electrically floating body of the thruster. This electrode was connected to a Keysight 34461A digital multimeter to read the potential, see Fig. 2. This body potential is important to measure as we perform our tests because it is a proxy to how the thruster behaves upstream near the discharge chamber.

VI. Results

We present in the following section key results from our parametric study. We first show our performance metrics of our ECR thruster as we varied the location of the steel sheet grounded to the chamber wall. We then present performance metrics as we varied the electrical bias of the suspended panel relative to chamber ground. Finally, we present current measurements taken from the panel, and thruster body potential measurements as we biased the sheet.

A. Performance for different locations of downstream boundary conditions

We present thrust measurements as we parametrically alter thruster input power, propellant flow rate, and downstream boundary location. We show thrust versus flow rate in figure 7 for the three different downstream panel locations in LVTF. For these tests, the panel was connected through an ammeter to chamber ground to simulate a chamber wall. At each panel location we measured thrust using a flowrate/power test matrix. This consisted of flow rates between 0.6-1.5 sccm and power between 20-26 Watts delivered to the thruster. We measured background pressure while the thruster was firing using the ion gauge located on the chamber wall. Results between different tests showed little variation between 2.5×10^{-7} Torr-xenon and 3×10^{-7} Torr-xenon.

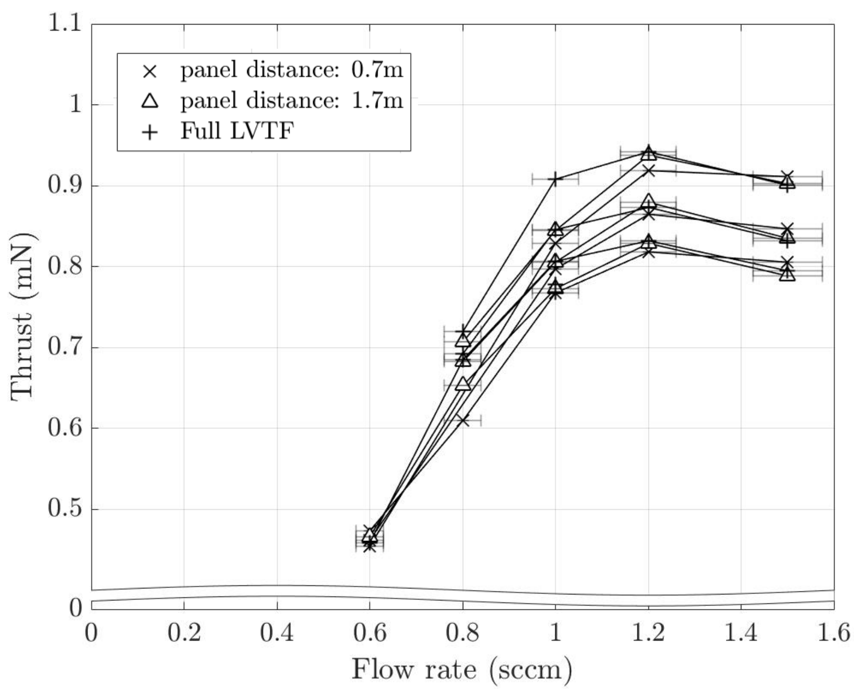

Fig. 7 Thrust measurements versus flow rate for the three panel locations inside LVTF. Connected points are the same input power swept from 0.6sccm to 1.5sccm.

Using these thrust measurements, we calculate thrust efficiency for the three different panel positions. We calculate this from the standard thrust efficiency formula:

$$\eta = \frac{F_T^2}{2\dot{m}P_{abs}}, \tag{1}$$

where F_T is the thrust force measured by the thrust stand, $\dot{m}$ is the mass flow rate, and P_{abs} is the total power absorbed by the thruster. This metric indicates how much thrust we can produce with a certain power input and mass flow rate.

We present in figure 8 efficiency vs flow rate per power absorbed by the thruster. This quantity was selected for the dependent coordinate based on previous work at ONERA showing measurements of specific impulse, thrust:power ratio, and efficiency could be fit to functions of a single variable [14]. The large uncertainty in these performance plots stems from high directivity error in the power mentioned in Sec. 2 and outlined in the appendix. This propagates through to efficiency. Error bars are shown on two points to show the magnitude of the uncertainty and are omitted from the remaining points for clarity.

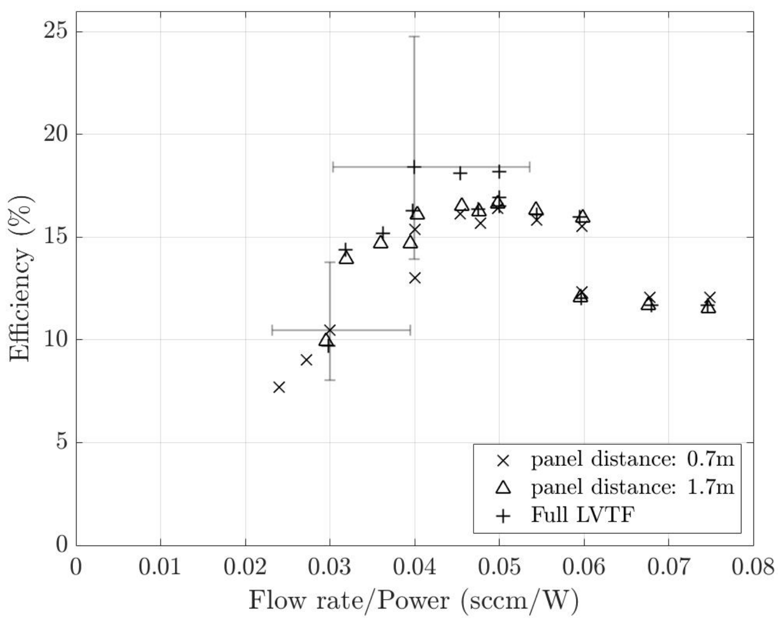

Fig. 8 Thrust efficiency versus flow rate per power absorbed by the thruster for the three panel locations inside LVTF.

Thrust measurements for the full LVTF configuration with no panel downstream are similar to those with the panel downstream, except for the 1 sccm flow rate where the thrust is observed to increase almost 10% when the panel is removed. This increase in performance with no panel in front of the thruster is indicative of the downstream boundary conditions playing a potential role in thruster behavior. The efficiency trends overall exhibit non-monotonic behavior. This showcases the sensitivity of these thrusters to what seems to be an optimal flow rate for a given power. Possible reasons for this include low ionization rates at low power density and attenuation of input power at high flow rates.

With that said, while efficiency also increases at at the 1 sccm flow rate; we note that this increase is within the associated uncertainty. The relatively large uncertainty here stems from the impact of uncertainty in estimating the power to thruster. Thus, we cannot draw the same direct conclusion about increase in efficiency with beam dump position as we do with the less ambiguous, higher pressure flow thrust measurements.

B. Performance as a function of panel bias

With this tentative confirmation of ONERA's results indicating performance dependence on chamber wall proximity, we seek to investigate the electrical configuration of the downstream panel as to explain this anomalous facility effect. To this end, we connected the steel panel to a DC power supply in order to bias it as shown in Fig. 2. We measured thrust as we biased the downstream panel from -200V to 200V for 1 sccm flow rate and 20W of input power to the thruster. The panel was located 0.7m downstream from the exit face of the thruster. We present these results and the efficiency measurements in figure 9.

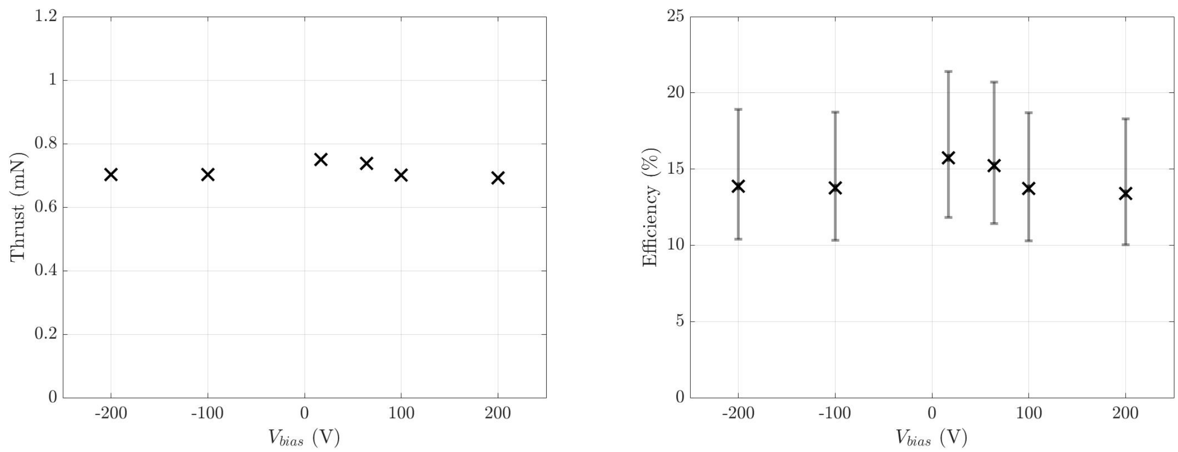

Fig. 9 (a) Thrust measurements and (b) thrust efficiency vs panel bias. Thruster firing on 1.0 sccm xenon at 20W input power.

As this result shows, we measured less than a 2% change in thrust between the extreme ends of the bias voltage. Efficiency calculations confirm that biasing the downstream sheet showed negligible performance changes from -200V to 200V with the sheet 0.7m away from thruster. This finding suggests that electrical bias of the downstream boundary may not be a driving factor in thruster performance.

C. Current as a function of panel bias

We consider the current collected by the beam dump at a location 0.7 m from the thruster as we varied the bias. While the beam dump was being actively biased, we measured current through the ammeter from the beam dump. We did this in order to determine the relative contributions of ion and electron current to thrust. As Fig. 10 shows, ion saturation was nearly achieved with approximately $-29mA$ at $-200V$ while the dump approached electron saturation with $23mA$ at $200V$. Interestingly, the electron current did not exceed the ion saturation current. This speaks at least qualitatively to the ambipolarity of the overall thruster, which globally must source as many positive as negative particles. We return to the implications of this result in Sec. 7. As the same time we applied the bias voltage, we also measured the thruster floating potential, which served as a proxy to upstream plasma potential. We found that the floating body potential of the thruster increased significantly when the panel is biased to electron collecting, see Fig. 11. This finding indicates that due to the downstream panel bias, plasma potential near the thruster is increasing. If this is the case, then we would expect to see some sort of change in thruster performance as the acceleration region of the thruster depends on this cascade of potential from the upstream plasma to the downstream plasma. Since we observe no change in performance, we postulate that the potential in the plume of the thruster is increasing everywhere at the same rate in order to accommodate the downstream boundary conditions. We return to this point in Sec. 7.

VII. Discussion

In this section we discuss the implications of our electrical study. In particular, our primary motivation is to try to elucidate why performance remained unchanged despite the 400 V change in panel bias. To this end, we develop a model for the current delivered to this source. We also briefly discuss the role of facility pressure on performance in the context of our results.

A. Implications of electrical study

Biasing the downstream panel allowed us to investigate how thruster performance and the discharge plasma change due to varying electrical boundary conditions. Intriguingly, biasing the sheet from -200V to 200V did not effect

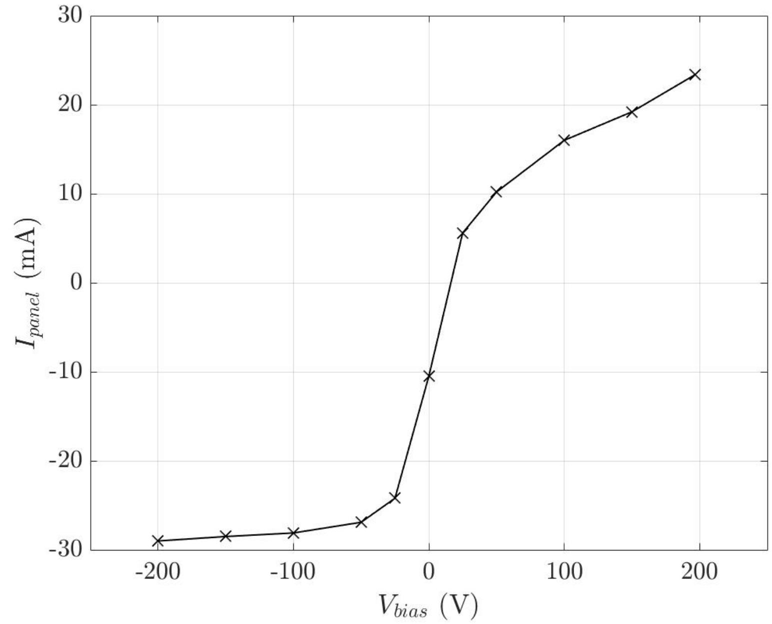

Fig. 10 Current through the panel versus panel bias. Thruster firing on 1.0 sccm xenon at 20W input power.

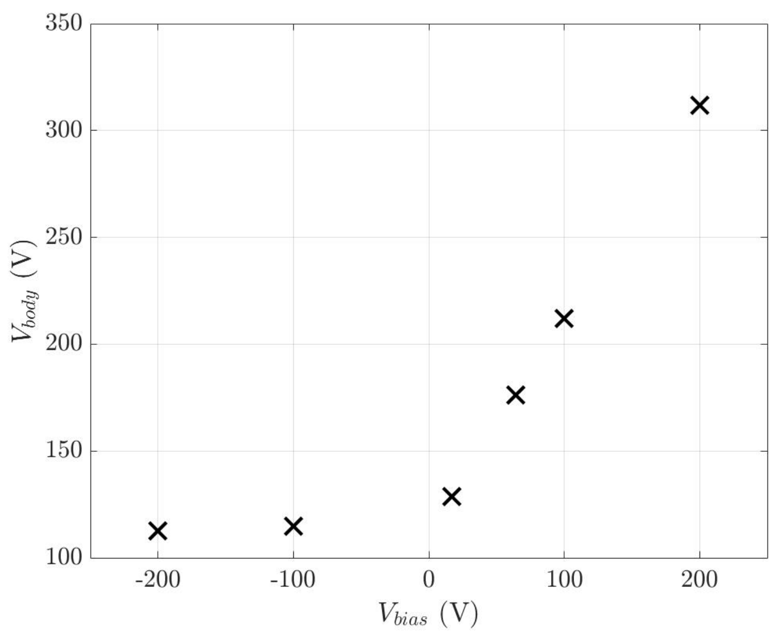

Fig. 11 Potential of the thruster body versus panel bias. Thruster firing on 1.0 sccm xenon at 20W input power.

performance. Ions deliver the bulk of the thrust to the thruster and the panel was biased to completely ion collecting with negligible change to thrust measurements. This could indicate that the majority of the acceleration region contributing to the overall thrust is within 0.7m downstream from the exit face with this boundary condition. The implementation of these boundary conditions could however affect the acceleration region. While the plate was biased to electron collecting, thruster body potential increased significantly. This is evidence for electrical accommodation of the downstream boundary condition. We postulate that the potential structure of the plume adjusts itself to maintain a set voltage between the plate and the thruster. It is possible that this adjustment is done once the plasma magnetically detaches as to not affect thruster performance. To investigate this further, we present a current model to illustrate this phenomenon.

1. Modeling of the current

Treating the plate as a double Langmuir probe biased relative to the chamber wall allows the extraction of downstream plasma properties within the plume. We follow conventional Langmuir probe theory outlined in [23] describing the current to the plate and wall, denoted by the subscript p and w respectively. Assuming a Maxwellian electron energy distribution we can write the currents as represented in VII.A.1 and VII.A.1.

$$I_p = I_{satp}(-1 + \sqrt{\frac{m_i}{2\pi m_e}} e^{q_e(V_p - \phi_p)/Te_p}) \tag{2}$$

$$I_w = I_{satw}(-1 + \sqrt{\frac{m_i}{2\pi m_e}} e^{q_e(V_w - \phi_w)/Te_w}) \tag{3}$$

Current is denoted by I, the subscript sat refers to the saturation current, m_i is the mass of a xenon ion, m_e and q_e is the mass and charge of an electron, V is the potential with respect to chamber ground effectively making $V_w = 0$ by definition. ϕ and T_e is the plasma potential and electron temperature near the plate or wall.
We consider our ECR magnetic nozzle thrusters to be ambipolar. In conjunction, they can only source so much current from the discharge plasma. Therefore in order to complete a circuit through the panel the amount of current to the panel for a certain species, either ions or electrons, must equal that of the opposite species on the chamber walls. This is represented mathematically with equations VII.A.1 and VII.A.1

$$I_p = I_w \tag{4}$$

$$I_{satp} = I_{satw} = 30mA \tag{5}$$

We assume a saturation current of 30 mA based on the current measured from the panel as we biased the voltage. With this current conservation in mind, we assume electrons are sufficiently far downstream and electron cooling is negligible that electron temperature at the wall and plate are the same $Te_p = Te_w = T_e$. Finally, we apply our hypothesis and allow the potential structure of the plume to adjust relative to the boundary conditions. This could be facilitated, for example, by a Boltzmann relation. For simplicity, we model this effect here by assuming a constant offset between the plasma potential near the wall and the plate.

$$\phi_p = \phi_w + \phi_{off} \tag{6}$$

We then solve for current to panel as shown in equation VII.A.1.

$$I_p = I_{sat} \tanh \frac{V - \phi_{off}}{2T_e} \tag{7}$$

We now have an equation for the current to the plate as a function of applied voltage to the plate. Electron temperature and the plasma potential offset will be treated as free parameters in order to fit to the current data of the panel. We implement a physical upper limitation of 24eV on electron temperature at the panel. We do this because Langmuir probe measurements (not reported here) upstream of the plasma at this thruster configuration show a temperature of $21.1 \pm 2.7eV$. We used a non-linear least squares method to fit equation VII.A.1 to the data. This yielded a plasma potential offset $\phi_{off} = 22.7V$ and an electron temperature $T_e = 24eV$. Figure 12 shows this fit overlaid on top of the IV data taken for the panel while it was located 0.7m downstream.

We remark here that there is excellent quantitative agreement with the lower part of the curve. The agreement diverges with higher bias voltage, however. This is likely due to the oversimplifying assumptions we have made about

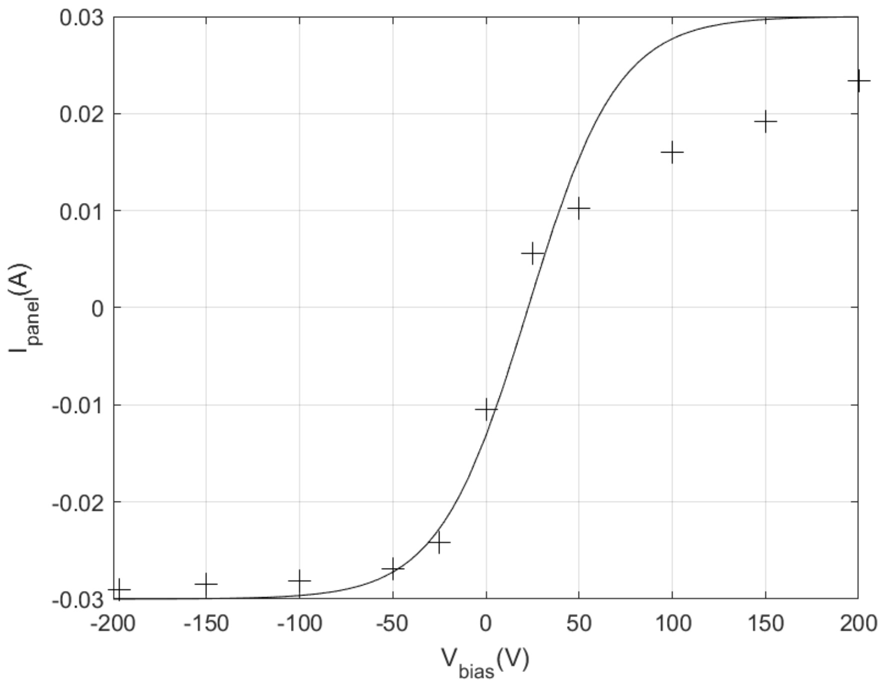

Fig. 12 Panel current versus panel bias. The best fit line is shown using ϕ_{off} and Te as free parameters.

the isothermality of electrons or the fact that the potential difference between plate and wall remains constant. In reality, both of these features likely are violated, which a higher fidelity model may capture. For the purpose of our discussion, however, the qualitative agreement at higher bias voltage still provide sufficiently high fidelity agreement to leverage this simplified model to further interpret our findings. Now that we have downstream plasma properties let us consider the upstream plasma properties. We treat our measurements of the floating thruster body potential as a proxy to the plasma potential upstream near the thruster. In order to find this change in potential near the thruster, we consider the plasma potential near the wall where $V_w = 0$. Assuming current conservation, the current to the wall is equal to the current inferred from our best fit analysis, as shown in VII.A.1.

$$I_{sat} \tanh \frac{V - \phi_{off}}{2Te} = I_{satw}(-1 + \sqrt{\frac{m_i}{2\pi m_e}} e^{-q_e \phi_w / Te}) \tag{8}$$

We then solve for plasma potential near the wall represented by ϕ_w.

$$\phi_w = -T_e \ln \sqrt{\frac{2\pi m_e}{m_i}} (1 - \tanh \frac{V - \phi_{off}}{2T_e}) \tag{9}$$

ϕ_{off} and Te are calculated from our best fit analysis. This leaves the plasma potential adjacent to the wall as a function of the potential applied to the plate. There must be a plasma potential increase from the wall to the thruster body, ϕ_{body}. The lack of performance change as panel bias changed means acceleration dynamics do not change significantly and thus this potential drop remains approximately the same. We assume $\phi_{body} \approx \phi_w + \phi_c$. Where ϕ_c represents the small potential change from the wall to the thruster body. Using $\phi_{off} = 22.66$ V and $Te = 24$ eV calculated from the fit to the IV curve data on the panel and ϕ_c as a free parameter, we compare to current data taken from the electrode placed on the thruster body. ϕ_c is found to be 13.65V using the non-linear least squares fitting method. We expect this value to be relatively small compared to the downstream bias as acceleration region remains largely unchanged. Figure 13 shows this comparison.

In summary, a model is presented following standard double Langmuir probe while allowing the potential structure of the plasma plume to change. The plasma potential difference between the panel and the wall and the electron temperature near the panel/wall was found by fitting the curve to the data collected from the beam dump. We then solve

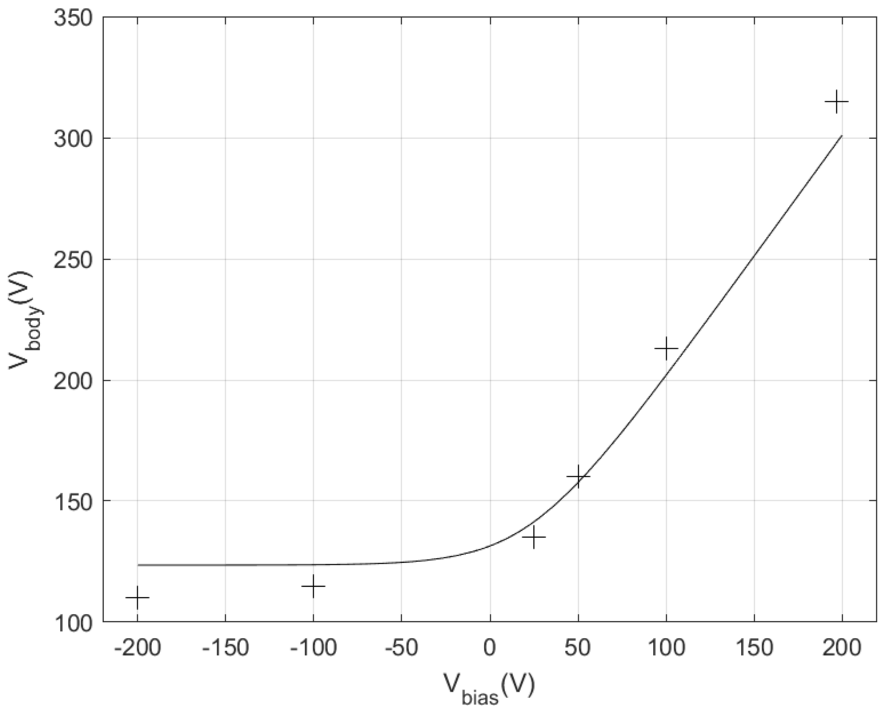

Fig. 13 Thrust body potential versus panel bias. The best fit line is shown using ϕ_c as a free parameter.

for the plasma potential near the wall using these values as a function of the voltage applied to the panel. Finally, we calculate plasma potential upstream near the thruster assuming a small potential change from the wall. This is in good agreement with the experimental data taken of the potential on the thruster body.

2. Implications for efficiency

In light of our preceding analysis, it is evident that the downstream electrical boundary conditions do affect the potential structure of the plume and in turn the potential of the thruster upstream. However, one interpretation for the fact that the thruster performance is unchanged is that the overall change in accelerating voltage from thruster to the downstream remains unchanged. Rather, the impact of increasing beam dump bias is simply to raise both potentials at both locations by the same amount. This increase is facilitated by the fact that ambipolarity demands that current at the walls balance current at the beam dump. With that said, it is notable that the thruster plume is able to respond this way, in what would appear to be a process described by a classical, double probe configuration. This speaks to the possibility that the downstream boundary conditions are sufficiently far from the thruster that the plasma is unmagnetized such that electrons and ions can migrate freely. Indeed, at 0.7 m, the magnetic field strength coming from the permanent magnets is negligible [20]. Thus, the majority of the field is dominated by the Earth's magnetic field which for our location is approximately 0.5 G [24]. The electron temperature obtained from (unreported) single Langmuir probe measurements was on average 20 eV for all 0.7 m thruster operating points. The corresponding electron Larmor radius at this magnetic field and electron temperature is approximately 30 cm, or 20× the size of the thruster. The plasma is thus likely demagnetized at this point and no longer effectively communicating thrust to the the upstream plasma.

B. Role of back pressure

The thruster performance does not seem to change as a function of electrical configuration of the downstream boundary conditions. If this is not the cause of the performance discrepancy seen in this study at 1sccm or from ONERA's study between different chambers, then we must reconsider facility pressure as a cause. For example, pressure read from the ion gauges at the wall could not be completely indicative of the local pressure the thruster sees. This stems from the marked distance between the ion gauge and thruster (see Fig. 5). With that said, there may be slight performance improvements as the steel sheet is removed from view of the thruster. This could indicate that there is some back pressure coming from the sheet affecting performance. This would not be resolved with the wall gauge. Similarly, in principle, the plasma that is reflected from the sheet would have lower energies as the sheet is much cooler than incident particles from the thruster. This would lead to a population of lower energy particles directly in front of the thruster. Collisions with this population of low energy particles could leech electron energy and therefore decrease ion kinetic energy resulting in lower thrust. With that said, we note that while this back pressure from the panel is a possibility, the relatively low flow rates from our thruster compared to the pumping speed of our facility suggest that it may be negligible.

C. Interpretation of results

The lack of performance change as a function of downstream boundary condition bias points to a mechanism in which the plasma plume will adjust itself relative to its boundary conditions. This adjustment seemed to raise plasma potential in the plume when the panel was biased to electron collecting, but it did not affect the acceleration region in which most of the thrust is generated. This could be because the plasma was detached from the magnetic field lines of the nozzle, allowing currents to freely adjust without affecting performance. Specifically, the plasma potential near the panel seems to increase as to prevent more electron current from flowing as the voltage of the panel increases. This in turn increases the plasma potential everywhere in the plume increasing body potential of the thruster.

VIII. Conclusions

We systematically investigated the role of electrical boundary conditions on the operation of an ECR magnetic nozzle thruster. We simulated a downstream chamber wall in front of our thruster in order to test varying chamber sizes. A tentative increase in performance is observed as we removed the steel foil panel from downstream of the thruster. This result is in agreement with that of ONERA's findings showing increased performance in a larger vacuum chamber at similar pressures. This indicates a facility effect in which chamber wall proximity affects thruster performance. We postulate this is due to the electrical configuration of the chamber walls. In order to test this, we biased our downstream panel while measuring performance metrics and various aspects of the thruster operation. We found that performance is insensitive to the downstream bias conditions. However, while performance remained unchanged, current from the plume of the thruster to the panel was shown to vary significantly. To explain this behavior, we hypothesized that the plasma potential increases everywhere within the plume as to accommodate the downstream bias. Thruster body potential also increased significantly while the panel was biased to electron collecting. We developed a current model by treating the panel as a double Langmuir probe biased relative to the chamber walls. By allowing the demagnetized plume to adjust itself to accommodate the downstream bias, we showed good agreement with experimental measurements of current through the biased panel and potential of the thruster body. This suggests the potential near the panel increases as to prevent more electron current from flowing as the voltage of the panel increases. In turn, this raises the potential everywhere including upstream near the thruster as to maintain a consistent acceleration region. Presumably, this is possible as the plasma is far enough downstream that the relative currents can adjust however they need to in order keep a set a voltage between the thruster and downstream panel.

Given that our results showed that downstream electrical bias does not appear to be a driving factor in performance, we also briefly discussed pressure within our chamber during testing. The operating pressure read from the ion gauge on the chamber wall did not show significant deviation during testing. However, the presence of the simulated chamber wall could have created a region of higher pressure directly in front of the thruster. While we deem this to be unlikely due to our relatively low flow rate compared to the testing facility pumping capabilities, it could potentially affect performance. Simulations are needed to access if the panel creates this pressure difference between the thruster and the ion gauge.

ECR magnetic nozzle thrusters have the potential to meet the demand for efficient, high specific impulse, low power propulsion. This study showcases the sensitive nature of these thrusters to their test environment. While the downstream electrical configuration of the chamber walls may not affect the performance of these thrusters, proximity of the walls may still be a factor limiting performance. Therefore future testing of these devices should be done with this in mind. Considering the results presented here and from previous studies, ideally, testing should be done at the lowest possible pressure in a high volume test facility.

Appendix

1. Thrust Uncertainty Analysis

We quantified direct thrust measurements using uncertainty analysis detailed in Ref. [20] and Ref. [25]. There are four primary contributions toward thrust uncertainty: random disturbances in the thrust stand displacement measurement (σ_δ), calibration slope uncertainty ($\sigma_{k_{cal}}$), geometrical tolerances of the thrust center to thrust stand pivot length (σ_{l_T}), and calibration weight center of mass to pivot length ($\sigma_{l_{cal}}$). The total thrust uncertainty is calculated using the root sum square statistical method:

$$\frac{\sigma_T}{T} = \sqrt{\left(\frac{\sigma_\delta}{\delta}\right)^2 + \left(\frac{\sigma_{k_{cal}}}{k_{cal}}\right)^2 + \left(\frac{\sigma_{l_T}}{l_T}\right)^2 + \left(\frac{\sigma_{l_{cal}}}{l_{cal}}\right)^2}, \tag{10}$$

Define all the variables in the

Individual uncertainty values for the thrust stand used are $\sigma_\delta = 8 \times 10^{-5}$ mm, $\sigma_{k_{cal}} = 5.8 \times 10^{-5}$ mm/mN, $\sigma_{l_T} = 1$ mm, and $\sigma_{l_{cal}} = 1$ mm [20],

2. Microwave Power Uncertainty Analysis

Uncertainty in microwave power arises from error in the power sensor (ΔP_{sensor}) and the directional coupler ($\Delta P_{directivity}$). The error in the N8482H power sensor is estimated as under 3% for our experiments [20]. While ΔP_{sensor} is a random error, $\Delta P_{directivity}$ is a systematic error that depends on the ratio of reflected power to forward power. The directivity error is approximated using Figure 14. The total power uncertainty is the sum of the two errors, given as

$$\Delta P_{abs} = \Delta P_{sensor} + \Delta P_{directivity}. \tag{11}$$

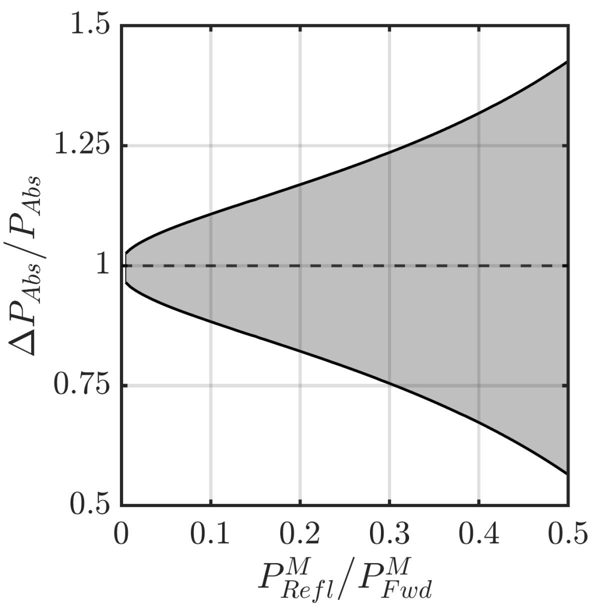

Fig. 14 Relative uncertainty in absorbed microwave power as a function of reflection coefficient. Reproduced from [20] with author permission.

3. Combining Thrust and Microwave Power Uncertainty

Error in thrust and microwave power propagate through efficiency calculations and the flow rate per absorbed power term that appears in forthcoming plots. While the power sensor error is random and can be applied using a quadrature uncertainty method, the directivity error is systematic and instead must be incorporated using a worst-case approach. The resulting minimum and maximum efficiencies are given in Equations VIII..3 and VIII..3, where P_{min} and P_{max} are calculated using the directivity errors found with Figure 14.

$$\eta_{min} = \frac{T^2}{2\dot{m}P_{max}} - \sqrt{\left(\frac{\partial\eta}{\partial T}\Delta T\right)^2 + \left(\frac{\partial\eta}{\partial\dot{m}}\Delta\dot{m}\right)^2 + \left(\frac{\partial\eta}{\partial P_{abs}}\Delta P_{sensor}\right)^2}, \tag{12}$$

$$\eta_{max} = \frac{T^2}{2\dot{m}P_{min}} + \sqrt{\left(\frac{\partial\eta}{\partial T}\Delta T\right)^2 + \left(\frac{\partial\eta}{\partial\dot{m}}\Delta\dot{m}\right)^2 + \left(\frac{\partial\eta}{\partial P_{abs}}\Delta P_{sensor}\right)^2}. \tag{13}$$

The partial derivatives here are given as

$$\frac{\partial\eta}{\partial T} = \frac{T}{\dot{m}P_{abs}}, \tag{14}$$

$$\frac{\partial\eta}{\partial\dot{m}} = -\frac{T^2}{2\dot{m}^2P_{abs}}, \tag{15}$$

$$\frac{\partial\eta}{\partial T} = -\frac{T^2}{2\dot{m}P_{abs}^2}. \tag{16}$$

Note the flow rate uncertainty is assumed to be 5%. Further details on this formulation are provided in Ref. [20]. The flow rate (in sccm) per absorbed power follows a similar formulation, given as

$$f_{min} = \frac{flow}{P_{max}} - \sqrt{\left(\frac{\partial f}{\partial flow}\Delta flow\right)^2 + \left(\frac{\partial f}{\partial P_{abs}}\Delta P_{sensor}\right)^2}, \tag{17}$$

$$f_{max} = \frac{flow}{P_{min}} + \sqrt{\left(\frac{\partial f}{\partial flow}\Delta flow\right)^2 + \left(\frac{\partial f}{\partial P_{abs}}\Delta P_{sensor}\right)^2}, \tag{18}$$

where

$$f = \frac{flow}{P_{abs}}. \tag{19}$$

The partial derivatives here are given as

$$\frac{\partial f}{\partial flow} = \frac{1}{P_{abs}}, \tag{20}$$

$$\frac{\partial f}{P_{abs}} = -\frac{flow}{P_{abs}^2}. \tag{21}$$

Acknowledgments

Thank you to Eric Viges and fellow members of the Plasmadynamics and Electric Propulsion Laboratory for their help with the Large Vacuum Test Facility procedures and insightful conversations.

References

[1] Jahn, R. G., *Electrodeless-Discharge Acceleration*, McGraw-Hill, Inc., 1968, pp. 134–139.

[2] Sercel, J. C., "An experimental and theoretical study of the ECR plasma engine," Ph.D. thesis, California Institute of Technology, 1993. https://doi.org/10.7907/PDWR-J354, URL https://resolver.caltech.edu/CaltechETD:etd-10192005-142203.

[3] Sheppard, A. J., and Little, J. M., "Scaling laws for electrodeless plasma propulsion with water vapor propellant," *Plasma Sources Science and Technology*, Vol. 29, No. 4, 2020, p. 045007. https://doi.org/10.1088/1361-6595/ab759e, URL https://doi.org/10.1088/1361-6595/ab759e.

[4] Conde, L., Domenech-Garret, J.-L., Donoso, J., Damba, J., Tierno, S., Gamboa, E., and Castillo Acero, M., "Supersonic plasma beams with controlled speed generated by the alternative low power hybrid ion engine (ALPHIE) for space propulsion," *Physics of Plasmas*, Vol. 24, 2017, p. 123514. https://doi.org/10.1063/1.5005881.

[5] Siddiqui, U., and Cretel, C., "Updated Performance Measurements and Analysis of the Phase Four RF Thruster," *2018 Joint Propulsion Conference, American Institute of Aeronautics and Astronautics*, 2018. https://doi.org/10.2514/6, URL https://arc.aiaa.org/doi/10.2514/6.2018-4817.

[6] Mazouffre, S., "Electric propulsion for satellites and spacecraft: established technologies and novel approaches," *Plasma Sources Science and Technology*, Vol. 25, No. 3, 2016, p. 033002. https://doi.org/10.1088/0963-0252/25/3/033002, URL https://doi.org/10.1088/0963-0252/25/3/033002.

[7] Navarro-Cavall, J., Ahedo, E., Merino, M., Ruiz, M., Ingenier, S., Ochoa, S., and del Amo, A. G., "Helicon Plasma Thrusters: prototypes and advances on modeling," 2013.

[8] Geller, R., *Electron Cyclotron Resonance Ion Sources and ECR Plasmas*, Routledge, 1996. https://doi.org/10.1201/9780203758663, URL https://doi.org/10.1201/9780203758663.

[9] Lieberman, M. A., and Lichtenberg, A. J., *Principles of Plasma Discharges and Materials Processing*, John Wiley & Sons, Inc., 2005. https://doi.org/10.1002/0471724254, URL https://doi.org/10.1002/0471724254.

[10] Hohl, M., Wurz, P., and Bochsler, P., "Investigation of the density and temperature of electrons in a compact 2.45 GHz electron cyclotron resonance ion source plasma by x-ray measurements," *Plasma Sources Science and Technology*, Vol. 14, No. 4, 2005, pp. 692–699. https://doi.org/10.1088/0963-0252/14/4/008, URL https://doi.org/10.1088/0963-0252/14/4/008.

[11] Miller, D., Gibbons, E., and Gloersen, P., "Cyclotron resonance propulsion system," *Electric Propulsion Conference, American Institute of Aeronautics and Astronautics*, 1963.

[12] Kuninaka, H., Nishiyama, K., Funaki, I., Yamada, T., Shimizu, Y., and Kawaguchi, J., "Powered Flight of Electron Cyclotron Resonance Ion Engines on Hayabusa Explorer," *Journal of Propulsion and Power*, Vol. 23, No. 3, 2007, pp. 544–551. https://doi.org/10.2514/1.25434, URL https://doi.org/10.2514/1.25434.

[13] Désangles, V., Packan, D., Jarrige, J., Peterschmitt, S., Dietz, P., Scharmann, S., Holste, K., and Klar, P., "ECRA thruster advances, H2020 MINOTOR project conclusion," *5th Workshop on MicroPropulsion and CubeSats*, Toulouse, France, 2021.

[14] Vialis, T., Jarrige, J., Aanesland, A., and Packan, D., "Direct Thrust Measurement of an Electron Cyclotron Resonance Plasma Thruster," *Journal of Propulsion and Power*, Vol. 34, No. 5, 2018, pp. 1323–1333. https://doi.org/10.2514/1.B37036, URL https://doi.org/10.2514/1.B37036.

[15] Wachs, B., and Jorns, B., *Effect of Background Pressure on Ion Dynamics in an Electron Cyclotron Resonance Thruster*, 2018. https://doi.org/10.2514/6.2018-4585, URL https://arc.aiaa.org/doi/abs/10.2514/6.2018-4585.

[16] Lafleur, T., "Helicon plasma thruster discharge model," *Physics of Plasmas*, Vol. 21, No. 4, 2014, p. 043507. https://doi.org/10.1063/1.4871727, URL https://doi.org/10.1063/1.4871727.

[17] Lafleur, T., Cannat, F., Jarrige, J., Elias, P. Q., and Packan, D., "Electron dynamics and ion acceleration in expanding-plasma thrusters," *Plasma Sources Science and Technology*, Vol. 24, No. 6, 2015, p. 065013. https://doi.org/10.1088/0963-0252/24/6/065013, URL https://doi.org/10.1088/0963-0252/24/6/065013.

[18] Boswell, R., Takahashi, K., Charles, C., and Kaganovich, I., "Non-local electron energy probability function in a plasma expanding along a magnetic nozzle." *Frontiers in Physics*, Vol. 3, 2015, 14. https://doi.org/10.3389/fphy.2015.00014.

[19] Cannat, F., Lafleur, T., Jarrige, J., Chabert, P., Elias, P.-Q., and Packan, D., "Optimization of a coaxial electron cyclotron resonance plasma thruster with an analytical model," *Physics of Plasmas*, Vol. 22, No. 5, 2015, p. 053503. https://doi.org/10.1063/1.4920966, URL https://aip.scitation.org/doi/abs/10.1063/1.4920966.

[20] Wachs, B. N., "Optimization and Characterization of Facility Effects for a Low-Power Electron Cyclotron Resonance Magnetic Nozzle Thruster," Ph.D. thesis, University of Michigan, 2022.

[21] Wachs, B., and Jorns, B., "Optimization of an ECR Thruster using Two Frequency and Pulsed Waveforms," *AIAA Propulsion and Energy 2021 Forum*, AIAA, 2021. https://doi.org/10.2514/6.2021-3382, URL https://arc.aiaa.org/doi/abs/10.2514/6.2021-3382.

[22] Eric A. Viges, A. D. G., Benjamin A. Jorns, and Sheehan, J. P., "University of Michigan's Upgraded Large Vacuum Test Facility," *36th International Electric Propulsion Conference*, Electric Rocket Propulsion Society, 2019. URL https://pepl.engin.umich.edu/pdf/IEPC-2019-653.pdf.

[23] Lobbia, R. B., and Beal, B. E., “Recommended Practice for Use of Langmuir Probes in Electric Propulsion Testing,” *Journal of Propulsion and Power*, Vol. 33, No. 3, 2017, pp. 566–581. https://doi.org/10.2514/1.B35531, URL https://doi.org/10.2514/1.B35531.

[24] Finlay, C. C., Maus, S., Beggan, C. D., Bondar, T. N., Chambodut, A., Chernova, T. A., Chulliat, A., Golovkov, V. P., Hamilton, B., Hamoudi, M., Holme, R., Hulot, G., Kuang, W., Langlais, B., Lesur, V., Lowes, F. J., Lühr, H., Macmillan, S., Mandea, M., McLean, S., Manoj, C., Menvielle, M., Michaelis, I., Olsen, N., Rauberg, J., Rother, M., Sabaka, T. J., Tangborn, A., Tøffner-Clausen, L., Thébault, E., Thomson, A. W. P., Wardinski, I., Wei, Z., and Zvereva, T. I., “International Geomagnetic Reference Field: the eleventh generation,” *Geophysical Journal International*, Vol. 183, No. 3, 2010, pp. 1216–1230. https://doi.org/10.1111/j.1365-246x.2010.04804.x, URL https://doi.org/10.1111/j.1365-246x.2010.04804.x.

[25] Polk, J. E., Pancotti, A., Haag, T., King, S., Walker, M., Blakely, J., and Ziemer, J., “Recommended Practice for Thrust Measurement in Electric Propulsion Testing,” *Journal of Propulsion and Power*, Vol. 33, No. 3, 2017, pp. 539–555. https://doi.org/10.2514/1.B35564, URL https://doi.org/10.2514/1.B35564.